Available online at www.sciencedirect.com
SCIENCE DIRECT®
Journal of Nuclear Materials 349 (2006) 265–281
journal of nuclear materials
www.elsevier.com/locate/jnucmat

Transmission electron microscopy examination of oxide layers formed on Zr alloys

Aylin Yilmazbayhan [a], Else Breval [a], Arthur T. Motta [a,*], Robert J. Comstock [b]

[a] *The Pennsylvania State University, Mechanical and Nuclear Engineering Department, 227 Reber Building, University Park, PA 16802, United States*
[b] *Westinghouse Electric Company, Science and Technology Department, 1340 Beulah Road, Pittsburgh, PA 15235, United States*

Received 14 July 2005; accepted 31 October 2005

Abstract

A transmission electron microscopy investigation was performed on oxides formed on three zirconium alloys (Zircaloy-4, ZIRLO and Zr–2.5Nb) in pure water and lithiated water environments. This research is part of a systematic study of oxide microstructures using various techniques to explain differences in corrosion rates of different zirconium alloys. In this work, cross-sectional transmission electron microscopy was used to determine the morphology of the oxide layers (grain size and shape, oxide phases, texture, cracks, and incorporation of precipitates). These characteristics were found to vary with the alloy chemistry, the corrosion environment, and the distance from the oxide/metal interface. These are discussed and used in conjunction with observations from other techniques to derive a mechanism of oxide growth in zirconium alloys.

1. Introduction

To ensure the safe and efficient operation of nuclear power plants, the stability and performance of the material used for nuclear fuel must be well understood. In pressurized water reactors, waterside corrosion of the cladding can limit the lifetime of the fuel, especially when the fuel is operated at high duty, for long residence times, and to high burnup. Although the cladding alloys currently used in nuclear power plants are adequate for current reactor operating conditions, alloys with greater corrosion resistance would allow for more challenging duty cycles, and further burnup extensions.

The oxide formed on Zr alloys has a protective nature, and therefore, the corrosion rate is determined by the properties of this oxide. It is well known that small differences in alloy microstructure and composition can lead to significant differences in corrosion behavior [1]. The work presented here is based on the hypothesis that these differences are related to microstructural differences in the oxides formed on different alloys. Following this hypothesis, the underlying reason for the corrosion differences may be found by studying the microstructure of the growing oxides.

* Corresponding author. Tel.: +1 814 865 0036; fax: +1 814 865 8499.
E-mail address: atm2@psu.edu (A.T. Motta).

0022-3115/$ - see front matter © 2005 Elsevier B.V. All rights reserved.
doi:10.1016/j.jnucmat.2005.10.012

The current study is part of a systematic effort to characterize a series of oxides formed on three different alloys in two environments using a variety of techniques. Examinations of these oxides with microbeam synchrotron radiation and transmitted light optical microscopy was previously reported [2,3]. The results of cross-sectional transmission electron microscopy of the same samples are presented in this paper. The results are compared to previous transmission electron microscopy examinations of Zr alloy oxides [4–9] and combined with previous results from microbeam synchrotron radiation and optical microscopy [3]. Finally, from the ensemble of these observations, conclusions are derived about the process of oxide film growth in zirconium alloys.

2. Experimental methods

2.1. Alloy materials

The alloys studied were Zircaloy-4, ZIRLO™, and Zr–2.5Nb fabricated into tubing from sponge-based ingots. The chemical analysis of the ingots is shown in Table 1. The fabrication of the tubing in the cold-worked and stress-relief-annealed condition was previously described [10]. In addition to tubing, sheet material of Zircaloy-4 and ZIRLO in the recrystallized condition was also included in this study. These alloys were selected for this study because of the wide differences in their corrosion behavior in pure and lithiated water autoclave environments.

2.2. Corrosion tests

Tube samples from these alloys were tested in 360 °C pure water at saturation pressure for up to 784 days. Sheet samples from Zircaloy-4 and ZIRLO were tested in 360 °C lithiated water for 242 days (Zircaloy-4) and 369 days (ZIRLO), while Zr–2.5Nb alloy tube samples were tested in the same environment for 3 days. The testing was performed in a manner consistent with standard procedures for testing zirconium-based alloys, as described in Standard ASTM G2-88. The lithiated water contained 70 ppm Li by weight added as lithium hydroxide. A set of archived samples taken at different stages of the corrosion tests was selected for examination to yield a more complete picture of the corrosion process.

Table 1
Chemical composition of zirconium alloy ingots (wt ppm)

Element	Zircaloy-4	ZIRLO	Zr–2.5Nb
Iron	2100	1000	504
Chromium	1000	<50	—
Copper	—	<25	<25
Niobium	—	9900	25500
Tin	15000	9600	10
Oxygen	1300	1430	1330
Zirconium	Balance	Balance	Balance

2.3. Sample preparation

The preparation of cross-sectional samples for examination by microbeam X-ray diffraction was described in an earlier publication [2]. Briefly, two axial segments of about 1.5 mm width were cut from the tubular corrosion samples and then ground from the inner diameter surface to a thickness of about 0.35 mm to facilitate subsequent insertion into a 3 mm diameter brass tube. The outer diameter oxide was placed next to the outer diameter oxide from a second axial slice. These pieces were glued together and inserted into a slot in a molybdenum rod. The molybdenum rod was inserted onto a 3 mm brass tube and glued in place by epoxy. Slices about 0.5 mm thick were cut from the brass tube to provide 3-mm diameter disks.

Mechanical grinding and polishing was performed to make TEM samples from these disks. The disk samples were ground on 600 grit SiC paper on both sides until the thickness was approximately 70–100 μm. One side of the disk was polished using progressively finer diamond abrasives to 0.5 μm diamond paste. The other side of the disk was then dimpled using a Gatan Model 656 Dimple Grinder with the dimple centered near the oxide–oxide interface. The dimple was made using diamond abrasives followed by a final polish using 0.05 μm alumina. The thickness of the disk at the bottom of the dimpled region was in the range of 5–8 μm.

The final thinning was performed using a Gatan Model 691 PIPS (Precision Ion Polishing System) instrument. Dimpled cross-sectional samples were milled from both sides with 5 keV Ar ions at an angle of 4–6° to decrease the milling rate and to maximize the electron-transparent regions. The samples were examined in a Philips 420 electron microscope operating at 120 keV at Penn State, and in a Philips CM-30 microscope operating at 300 keV at Westinghouse Electric Company.

3. Experimental results

3.1. Autoclave corrosion results

Fig. 1 shows the corrosion weight gains as a function of time for the three alloys. When tested in pure water, Zr–2.5Nb alloy exhibits the lowest corrosion rate, followed by ZIRLO and Zircaloy-4. In contrast, when tested in lithiated water, Zr–2.5Nb alloy has the highest corrosion rate and ZIRLO has the lowest. In the pure water environment, the first oxide transitions can be seen as changes in the corrosion rate (see arrows). The thickness at transition, calculated from the weight gain (15 mg/dm^2 corresponds to 1 μm of oxide) is shown in Table 2. The oxides that had the greatest transition thicknesses had the lowest post-transition corrosion rate [3].

3.2. Morphology of the oxide layers

Low magnification micrographs were taken to investigate the macrostructure of the oxide layers.

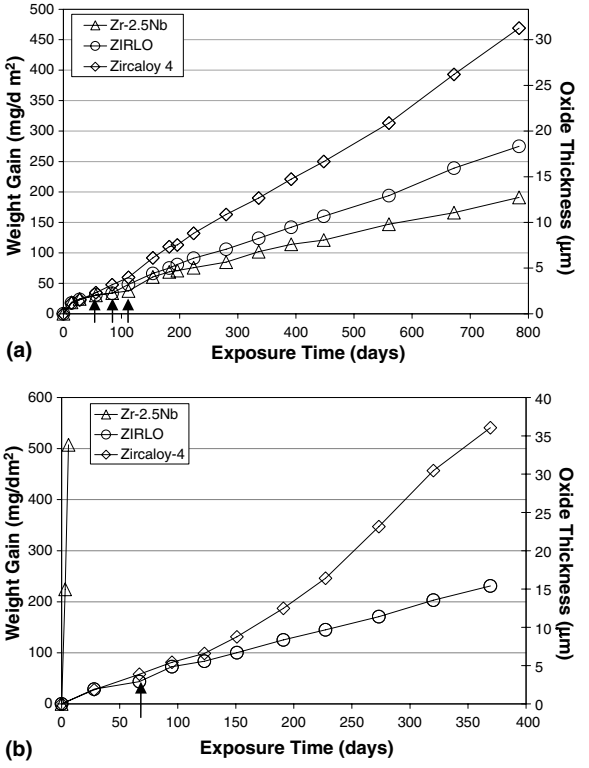

Fig. 1. Corrosion weight gain vs. exposure time of Zircaloy-4, ZIRLO and Zr–2.5Nb in (a) 360 °C pure water (solid arrows show the transition) and (b) 360 °C lithiated water (solid arrow shows the transition in ZIRLO, transition is not discernible in Zircaloy-4 and Zr–2.5Nb).

Fig. 2(a) and (b) shows low magnification bright-field transmission electron micrographs from oxides formed on ZIRLO and Zircaloy-4 in pure water. The micrographs show periodic lateral cracks in the oxide layers. The period was roughly constant throughout the oxide layer. The average distance between the cracks was 2.3 and 1.8 μm in oxides formed on ZIRLO and Zircaloy-4, respectively.

This periodicity has been observed in these oxide layers using other techniques (diffraction intensity variations observed with microbeam synchrotron radiation, transmitted light optical microscopy, etc.). Table 2 shows the period thicknesses measured by transmitted light microscopy, micro X-ray diffraction [3] and transmission electron microscopy (distance between the lateral cracks) and the first transition thickness evaluated from the change in slope in corrosion weight gain data. The different measurements yield similar transition thicknesses, which are then considered to be characteristic of the alloy and of the corrosion environment.

This periodicity was less evident in lithiated water. Fig. 2(c) and (d) shows low magnification bright-field transmission electron micrographs from oxides formed on ZIRLO and Zr–2.5Nb alloys in lithiated water. Although the ZIRLO alloy oxide shows periodicity in the lateral cracking, the oxide layer on the Zr–2.5Nb alloy does not show discernible periodicity despite the presence of many cracks; this was also true of Zircaloy-4. It is interesting to note that in ZIRLO, although the corrosion rate is higher in lithiated water than in pure water, the oxide transition thickness is larger in lithiated water than in pure water.

Both large columnar grains and small equiaxed grains were observed in the oxides studied. The oxide region around cracks such as those shown in Fig. 2 exhibits more equiaxed grains than are present in the bulk of the oxide. Fig. 3 shows three different bright-field micrographs from (a) ZIRLO oxide formed in lithiated water, (b) ZIRLO and (c) Zircaloy-4 oxides formed in pure water. The equiaxed grains are associated with cracks and the columnar grains are observed away from the cracks, similar to the results of Anada and Takeda [9] and Wadman et al. [6]. Fig. 3(d) is a bright-field image from ZIRLO oxide formed in pure water, which shows columnar grains on either side of a region of equiaxed grains. This equiaxed region is also the thinner (lighter) region in the image. The association of the cracks with equiaxed grains can be explained by the equiaxed grain region being more

Table 2
Oxide periodicity from different techniques

		Thickness/Time to transition (from weight gain)	Post transition corrosion rate (mg/dm^2/d)	Layer period		
				XRD*	Transmitted light*	TEM
Zircaloy-4	Water	1.6 ± 0.4 μm/28 days	0.58	1.9 ± 0.5 μm	1.9 ± 0.05 μm	1.9 ± 0.2μm
	Li (strip)	Not discernible	2.02	None	None	Not examined
ZIRLO	Water	2.3 ± 0.3 μm/84 days	0.33	2.3 ± 0.5 μm	2.1 ± 0.1 μm	2.3 ± 0.1 μm
	Li (strip)	2.7 ± 0.7 μm/67 days	0.59	3.1 ± 0.6 μm	2.8 ± 0.3 μm	2.8 ± 0.5 μm
Zr–2.5Nb	Water	2.5 ± 0.3 μm/112 days	0.21	3.1 ± 0.5 μm	2.8 ± 0.3 μm	2 ± 1 μm
	Li	Not discernible	84.6	None	None	Not periodic

* Refs. [2,3].

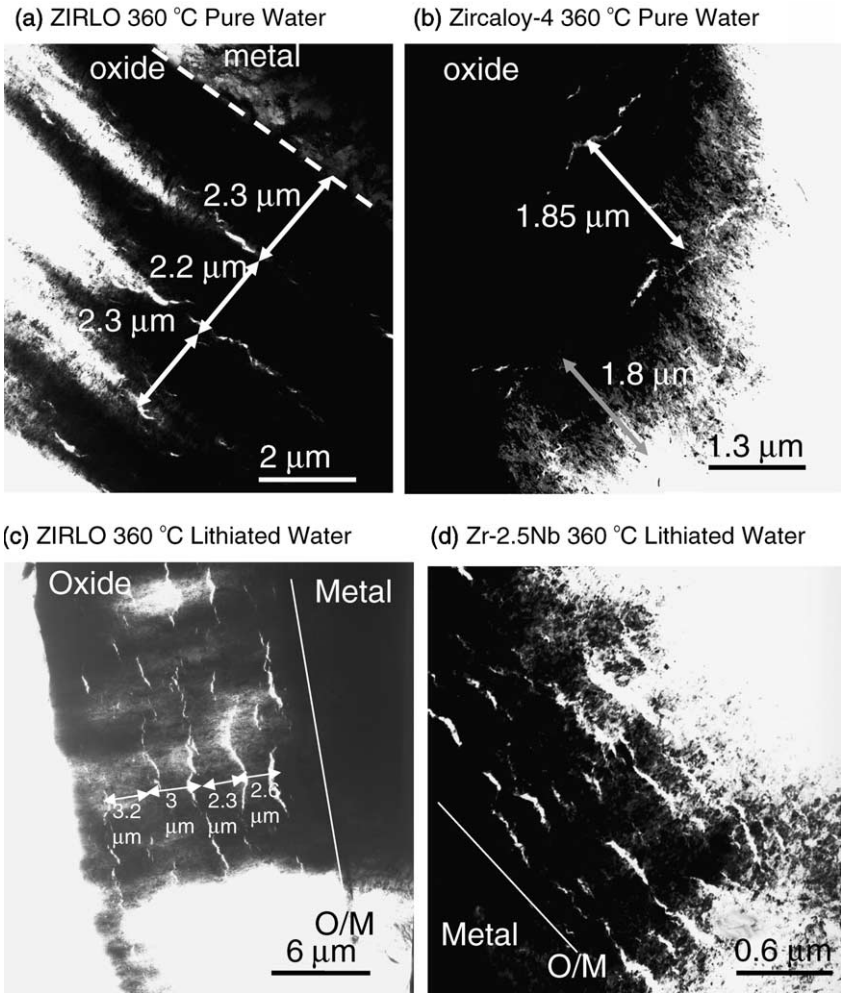

Fig. 2. Low magnification bright-field transmission electron micrographs in (a) ZIRLO, (b) Zircaloy-4 alloy oxides formed in 360 °C pure water environment for 784 days, and (c) ZIRLO, (d) Zr–2.5Nb in 360 °C lithiated water environment for 369 and 3 days, respectively.

susceptible to ion milling, or the cracks could be formed by a greater tendency of the equiaxed grains to crack during stress relief upon cooldown from the autoclave test temperature. It is also observed that grain decohesion occurred more frequently between the small equiaxed, short-narrow columnar grains

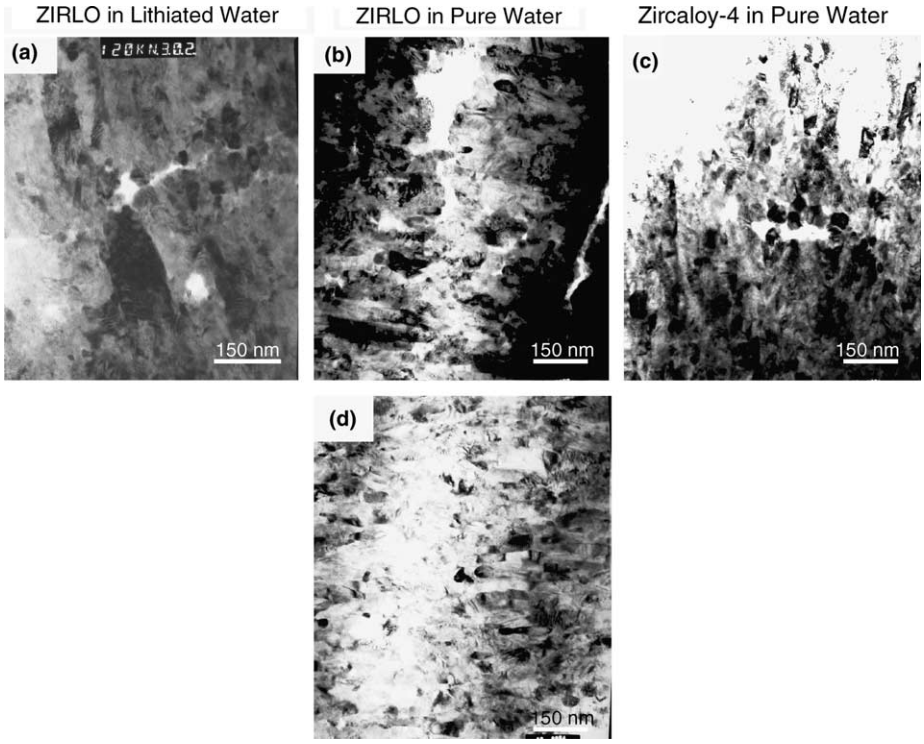

Fig. 3. Grain size comparison around the cracks of (a) ZIRLO alloy oxide in 360 °C lithiated water, (b) ZIRLO and (c) Zircaloy-4 alloy oxides formed in 360 °C pure water and (d) columnar–equiaxed–columnar type grain structure in ZIRLO alloy oxide formed in 360 °C pure water.

than between the wide and long columnar grains. Thus the cracks are likely an artifact of either ion milling or thin foil sample preparation.

Nevertheless, according to this hypothesis, the cracks show the location of the equiaxed grains. This would imply an alternation of columnar and equiaxed grains in the oxide layer such as seen in Fig. 3(d). This type of columnar to equiaxed to columnar grain shape variation was also observed by Doriot [11] in Zr–1NbO alloy oxide formed in steam.

In the outer part of the oxide (oxide/water interface), the equiaxed grain density is higher than in the rest of the oxide. In most of the oxide layer, columnar oxide grains are observed oriented in the direction perpendicular to the oxide/metal interface. This structure seen in the middle of the oxide extends all the way to the oxide/metal interface (interrupted periodically by thin equiaxed grain layers such as shown in Fig. 3(d)). The oxide/metal interface is well-defined for Zr–2.5Nb and ZIRLO and less well-defined for Zircaloy-4.

When the morphology of the columnar grains in the different alloy oxides is examined in more detail, distinct differences are observed. Fig. 4 shows three bright-field images taken from the oxides near the oxide/metal interface of Zircaloy-4, ZIRLO and Zr–2.5Nb alloys corroded in pure water and hand-drawn traces of the grain boundaries in these images. The columnar grain size and shape change according to the alloy. The length of the grains cannot be measured precisely because of grain overlap, but, in general, the narrower the grains, the shorter they are (the aspect ratio is about constant and of the order of five).

In the oxide formed on Zircaloy-4 (Fig. 4(a)), both equiaxed and columnar grains were observed, with the columnar grain width between 10 and 28 nm. The equiaxed-grain diameters range from 5 to 20 nm. In ZIRLO (Fig. 4(b)), the shapes of oxide grains are mainly columnar, but a few equiaxed grains are also observed. The width of the columnar grains is 25–33 nm and the diameter of the equiaxed grains is 17–24 nm. In Zr–2.5Nb oxide (Fig. 4(c)), the columnar oxide grains are wider and longer than that in the other alloys, and the equiaxed grain density is much lower than that in the other alloy oxides. The range of the columnar grain width is

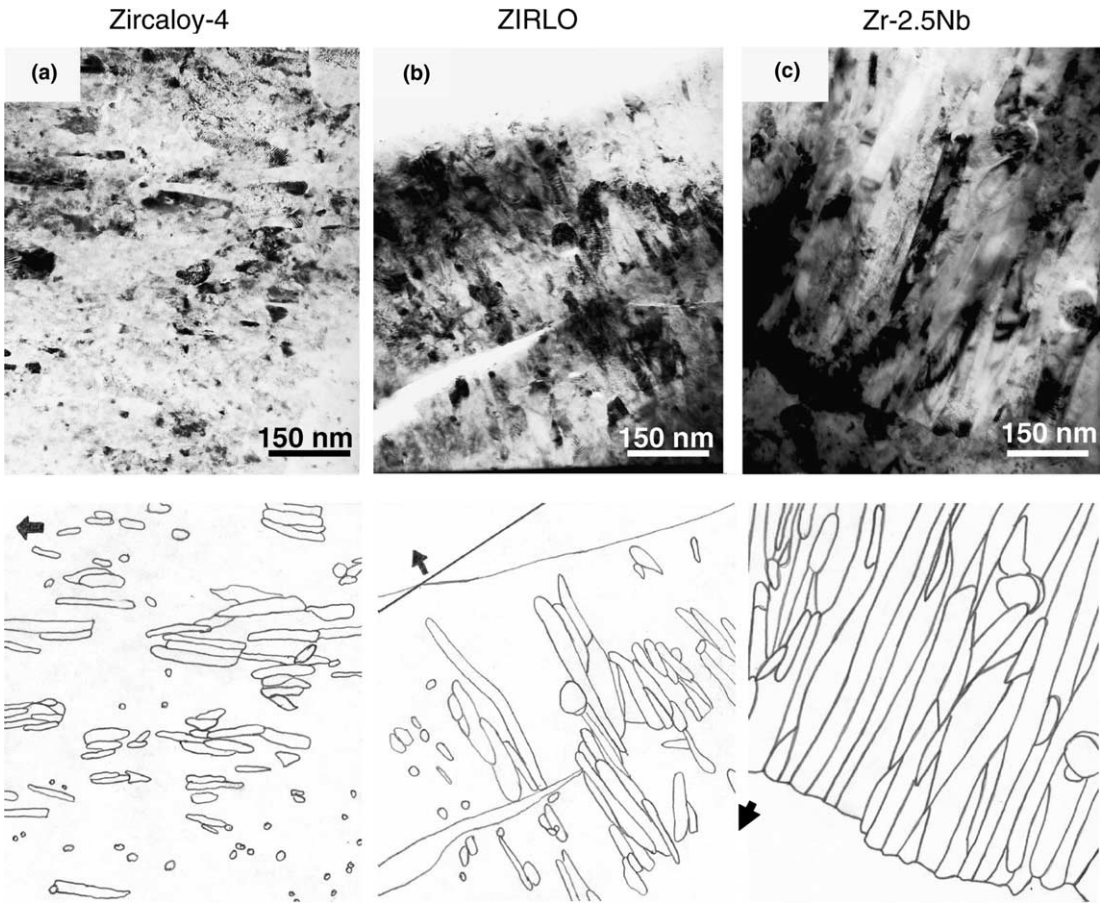

Fig. 4. Grain size, shape and orientation comparison near the oxide/metal interface of (a) Zircaloy-4, (b) ZIRLO and (c) Zr–2.5Nb alloy oxides formed in 360 °C pure water environments. The cartoons below each bright-field images show the hand-drawn sketch of the grain boundaries. (Black arrows indicate oxide growth direction.)

23–58 nm and the range of the diameter of the equiaxed grains is 14–28 nm.

The regions shown in Fig. 4(a)–(c) respond differently to tilt in the microscope. In general the grains in Zr–2.5Nb respond to tilting as a group, that is, diffraction contrast changes collectively for the majority of the grains, indicating small grain-to-grain misalignment. For Zircaloy-4 the grains respond to tilting individually, lighting up and becoming dark independent of each other indicating a greater degree of grain-to-grain misorientation. This means the columnar grains in the Zr–2.5Nb oxide are well-oriented with respect to each other, as demonstrated by their more collective response to tilting than shown by Zircaloy-4. The degree of alignment of the columnar grains in ZIRLO is intermediate between Zircaloy-4 and Zr–2.5Nb.

In contrast, the oxide layer formed in Zr–2.5Nb in lithiated water environment shows mainly equiaxed grains, significant grain decohesion and many small cracks between the equiaxed grains. Fig. 5 shows two bright-field images from Zr–2.5Nb alloy oxide formed in pure and lithiated water environments which illustrate the above contrast.

In summary, alloy oxides with lower corrosion rates exhibit large, more well-oriented columnar grains whereas alloy oxides with higher corrosion rates exhibit smaller equiaxed grains and smaller misoriented columnar grains. These observations suggest that the columnar grains are more protective against further oxidation.

The size of these oxide grains were also calculated from the line broadening of the various diffraction peaks in microbeam X-ray diffraction patterns using the Scherrer formula [3]. In the following discussion $(hkl)_M$ refers to monoclinic ZrO_2 planes and $(hkl)_T$ refers to tetragonal ZrO_2 planes. Table 3 shows the comparison of the grain size determina-

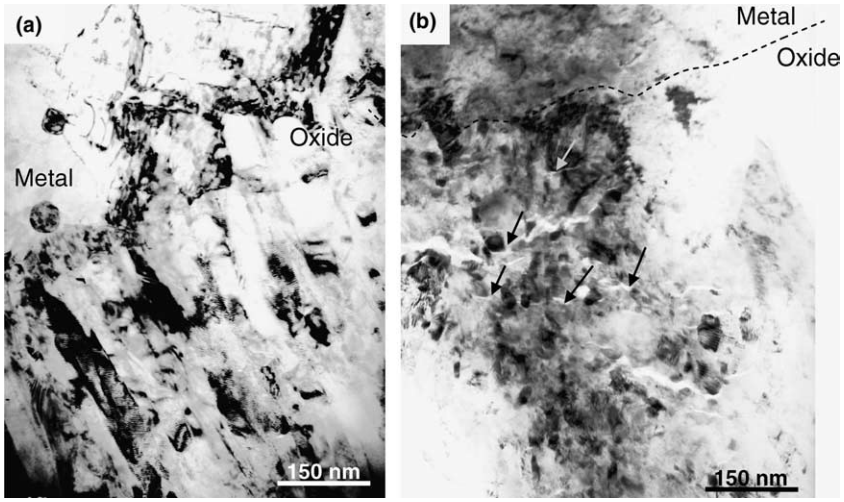

Fig. 5. Comparison of grain size and structure between Zr–2.5Nb in (a) 360 °C pure water and (b) 360 °C lithiated water.

Table 3
Oxide grain sizes (nm) measured by transmission electron microscopy and calculated from line broadening of the corresponding diffraction peaks $(hkl)_{M,T}$ *[2]

		Grain size in oxides formed in 360 °C pure water (nm)	Grain size in oxides formed in 360 °C lithiated water (nm)
Zircaloy-4	Size measured from $(1\,1\,1)_M$ line broadening*	19.8 ± 1	21 ± 1
	Columnar grain width	10–28	N/A
	Size measured from $(1\,0\,1)_T$ line broadening*	7.6 ± 0.6	7.6 ± 1
	Equiaxed grain diameter	5–20	N/A
ZIRLO	Size measured from $(1\,1\,1)_M$ line broadening*	21 ± 1	20.9 ± 0.3
	Columnar grain width	25–33	19–24
	Size measured from $(1\,0\,1)_T$ line broadening*	7.8 ± 1.2	8.6 ± 0.5
	Equiaxed grain diameter	17–24	10–19
Zr–2.5Nb	Size measured from $(1\,1\,1)_M$ line broadening*	27.5 ± 3	19 ± 1
	Columnar grain width	23–58	14–19
	Size measured from $(1\,0\,1)_T$ line broadening*	8 ± 4	7.7 ± 0.7
	Equiaxed grain diameter	14–28	14–19

N/A indicates no data available.

tion using transmission electron microscopy in this study and using line broadening of the diffraction peaks in a previous study [2]. The width of the columnar grains calculated from broadening of the $(1\,1\,1)_M$ peak is close to that observed for the columnar grains in TEM suggesting an association of the monoclinic phase with the columnar grains. However, the grain size calculated from the broadening of the $(1\,0\,1)_T$ peak is smaller than the measured size of the equiaxed grains in TEM. There are various possible reasons for this difference: (i) strain could contribute to the broadening observed with synchrotron radiation; (ii) it is likely that the equiaxed grains are a mixture of tetragonal and monoclinic grains, and (iii) the grain size distribution in TEM is skewed towards the larger grains, as those are easier to see. Finally, the average grain sizes in TEM were determined by measuring only a few tens of grains, and so the determination of grain size in the TEM has worse statistics than the same determination performed by line broadening measurement. Overall the measurements are consistent with the idea that the tetragonal grains are predominately small equiaxed and the monoclinic grains are predominately columnar.

3.3. Oxide texture

The crystallographic texture of the oxide layer and its variation with distance from the oxide/metal

interface were studied using electron diffraction. Electron diffraction patterns were taken from the region near the oxide/metal interface and contrasted with patterns taken far from the interface, into the bulk of the oxide. To obtain these patterns, large diffraction apertures (encompassing approximately 0.7 μm) were used, with the intent of obtaining a representative average of the texture evolution in the oxide layer.

The diffraction patterns were indexed using the established powder diffraction files for monoclinic (37-1484) and tetragonal ZrO_2 (42-1164), after calibration using a gold standard. The indexing for the oxide reflections were in good agreement with the previous indexing of X-ray diffraction patterns obtained with synchrotron radiation [3]. The locations of the monoclinic reflections measured by synchrotron radiation corresponded quite well with the powder diffraction file, while the tetragonal reflection $(101)_T$ (the only tetragonal reflection visible) was off by about 0.4° at 9 keV [2]. The indexing shows a preponderance of the monoclinic ZrO_2 phase over the tetragonal phase in the oxide layer, as well as the presence of hcp Zr metal peaks and hydride peaks in the pattern taken near the oxide/metal interface.

Fig. 6 shows two patterns taken from near and far from the oxide/metal interface of Zircaloy-4 oxide formed in pure water. In cross-sectional TEM sample geometry, the diffracting planes have their diffraction vectors perpendicular to the incoming beam. The main reflections of interest are the monoclinic reflections $(111)_M$, $(\bar{1}11)_M$, $(200)_M$, $(020)_M$ and $(002)_M$ and the tetragonal reflection $(101)_T$. The $(200)_M$ and $(020)_M$ monoclinic reflections are too close to be resolved in electron diffraction. The indexing of an observed diffraction peak at this two-theta position (deciding between $(200)_M$ and $(020)_M$) also takes into account information from a previous synchrotron radiation study [3], as explained below.

An intensity variation is visible along the arc of the $(\bar{1}11)_M$ and $(111)_M$ reflections in both diffraction patterns. Analysis of the intensity variations shows that the $(\bar{1}11)_M$ poles are oriented preferentially in a direction approximately 30–45° away from the oxide surface normal and that the $(111)_M$ poles are oriented about 50–60° away from the oxide surface normal. Texture measurements performed by Béchade and co-workers [12–14] in frontal X-ray diffraction geometry show the $(\bar{1}11)_M$ pole was strongest at 50° away and the $(111)_M$ pole strongest at 60–70°, from the oxide surface normal, in qualitative agreement with observations in this study.

Examining the $\{200\}_M$ family of peaks in the diffraction pattern taken near the oxide/metal interface region (Fig. 6(a)), the $(200)_M$ poles are oriented nearly parallel to the oxide growth direction and the $(002)_M$ poles are oriented approximately perpendicular to the oxide growth direction. The pole aligned close to the growth direction of the oxide is identified as $(200)_M$ because of information from previous synchrotron radiation

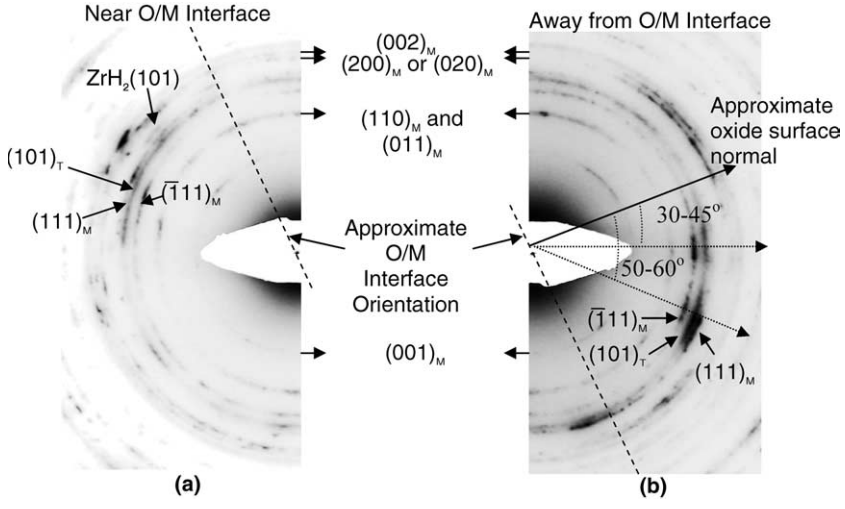

Fig. 6. Electron diffraction patterns taken from (a) the oxide/metal interface and from (b) the bulk of the oxide away from oxide/metal interface in Zircaloy-4 oxide formed in 360 °C pure water.

experiments which indicate the $(200)_M$ poles are aligned about 10° from the surface normal (in the oxide growth direction). Fig. 6(b) shows a similar but better developed texture. The intensity variation of the $(200)_M$ reflection indicates heavy texture with these planes oriented nearly parallel to the oxide/metal interface, while the $(002)_M$ planes are oriented perpendicular to the oxide/metal interface. The above peak identification agrees qualitatively with the microbeam X-ray diffraction observation if this reflection is interpreted as $(200)_M$ [3]. Information from transmission synchrotron radiation diffraction experiments indicates that the $(002)_M$ poles are aligned preferentially along either the axial or circumferential direction of the cladding. Thus, the texture of the monoclinic phase becomes more well-defined as we move from the oxide/metal interface to the bulk of the oxide. These observations were consistently made on several oxide samples and did not vary from location to location in the oxide.

The tetragonal ZrO_2 reflection $(101)_T$ is also observed in the electron diffraction patterns. The tetragonal reflection can be distinguished from the other reflections because of its more diffuse appearance compared to the monoclinic peaks. This could be caused by small grain sizes and/or by microstrains in the material. Compared to the monoclinic planes, the $(101)_T$ planes are oriented more randomly in the pattern as seen from the wide arc where its intensity is strong. However, the $(101)_T$ plane normal is the strongest in the angular range where the $(\bar{1}11)_M$ and $(111)_M$ reflections are also strong (40–70° away from the oxide surface normal). That is, the $(101)_T$ peak is more or less aligned in between the $(\bar{1}11)_M$ and $(111)_M$ reflections, i.e. around 45° from the oxide surface normal, as seen in Fig. 6(b). The tetragonal reflection was considerably stronger in the Zircaloy-4 samples than in ZIRLO and Zr–2.5Nb, indicating a higher tetragonal fraction, in agreement with previous results [2,3].

3.4. Oxide/metal interface region

The interface region in the growing oxide is of special interest, because this is the region where new oxide is formed, and which may control oxide growth. In this work, several features were observed that were particular to the oxide/metal interface region. Three characteristics are distinguished: the oxide grain structure and orientation at the interface, the interface itself and the presence of an oxygen-rich region ahead of the oxide front.

The interface is clearly seen in Zr–2.5Nb, where the large columnar grains form a well-defined interface. Fig. 7(a) and (b) shows two bright-field images from the oxide/metal interface of Zr–2.5Nb alloy oxide formed in pure water. Starting on the metal side of the oxide/metal interface, blockish, squarish, suboxide grains (100–150 nm wide rectangular grains) are observed. These blocky grains observed on the metal side of the oxide/metal interface are different from the equiaxed metal grains seen away from the oxide/metal interface, in Fig. 7(c).

The composition of the region in the metal near the oxide/metal interface was studied using energy dispersive X-ray spectroscopy with a 5–8 nm spot size. By moving the small focused beam on the sample with small step sizes (50–100 nm), a series of point spectra were collected from the oxide/metal interface to a certain distance into the metal. Using the Cliff–Lorimer technique, the atomic concentration of oxygen in the sample was determined, based on the Zr L and O K_α peaks. The tilting angle of the sample (14°) was taken into account, but possible sample thickness variations were not. Fig. 8 shows the measured oxygen content near the oxide/metal interface for oxides formed in 360 °C pure water in (a) Zircaloy-4 and (b) Zr–2.5Nb alloy. The solid line in the oxide is close to the theoretical level of oxygen in ZrO_2 (66.7 at.%) and the solid line in the metal to the theoretical solid solution limit of oxygen in α-Zr (29 at.%), as expected. It is clear that there is a significant increase above the oxygen solubility limit near the interface.

In Zircaloy-4, the oxygen content decreases smoothly from the oxide/metal interface. The oxygen content becomes lower than the solid solution limit (29 at.%) at a distance of 500–650 nm away from the oxide/metal interface. In Zr–2.5Nb oxide, oxygen content in the suboxide region decreases from 65 to 30 at.% within 100–200 nm from the interface. In Zr–2.5Nb and Zircaloy-4, oxygen content measurements were performed twice in the same region at locations separated from each other by 100–250 nm (the diamonds show the first measurement and the squares show the second measurement). The measurements are in agreement with each other, showing good reproducibility. This oxygen-rich region was the widest in Zircaloy-4, followed in order by ZIRLO and Zr–2.5Nb. Thus, the slowest moving oxides exhibited the smallest

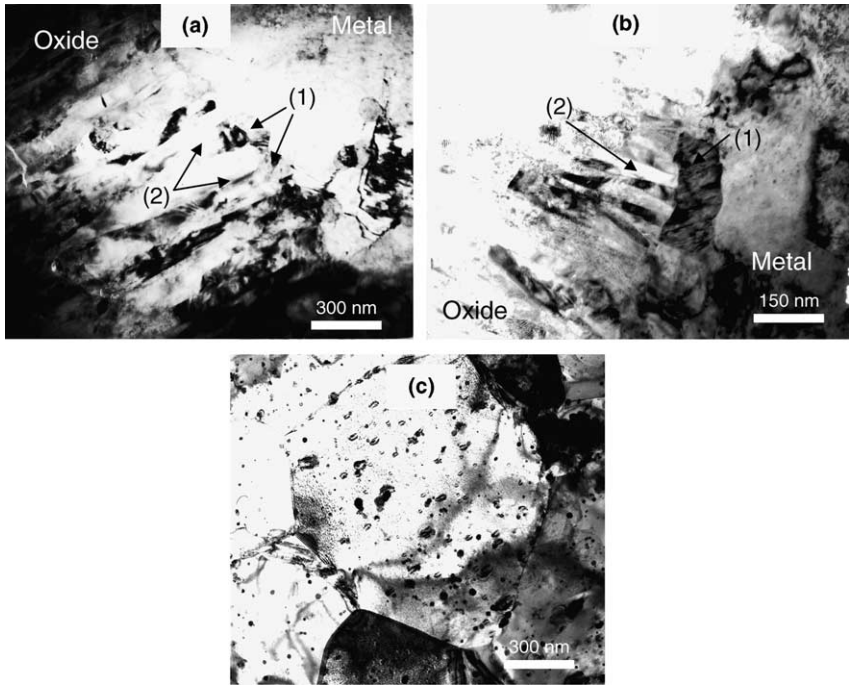

Fig. 7. Blocky 'suboxide' grains at the oxide/metal interface of Zr–2.5Nb alloy oxide formed in 360 °C pure water. These blocky grains (a, b) are different from the equiaxed metal grains observed in the metal far from the oxide/metal interface (c). (1) Blocky suboxide metal grains, (2) columnar oxide grains near interface.

oxygen-rich regions. Because these examinations are only a 'snapshot', it is not clear whether these differences are due to the different alloys, or to different stages in the corrosion process.

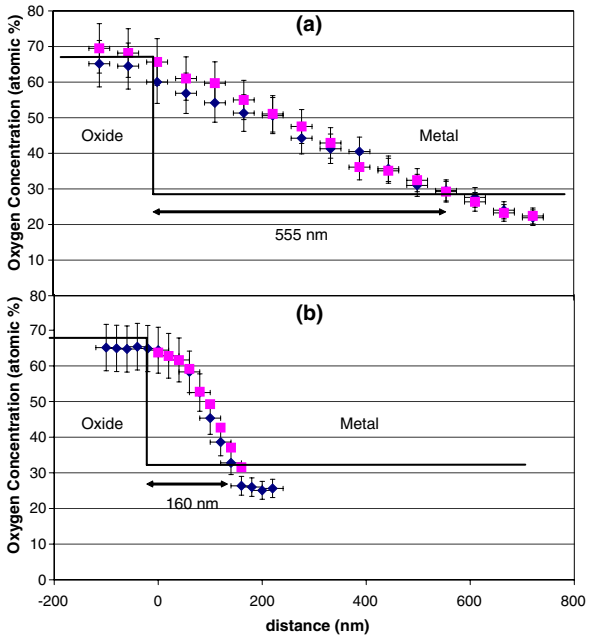

Fig. 8. Measured oxygen content from (a) Zircaloy-4 and (b) Zr–2.5Nb oxides formed in 360 °C pure water environment using EDS point spectra in TEM.

Although the extent of this oxygen-rich region varies between the alloys, it coincides in each case with the extent of the region showing blocky grains. This suggests that this region is a suboxide region formed ahead of the advancing oxide. The suboxide is a metastable ordered solution of O in Zr. Although no suboxide diffraction peaks could be clearly indexed in TEM (the peaks are very close to those of hcp Zr), Zr_3O suboxide peaks were identified in the same oxides using microbeam synchrotron radiation diffraction near the oxide–metal interface [3].

This blocky grain, oxygen-rich region exhibited a further difference from the bulk of the metal, in that within these grains fine particles were observed. The diffraction patterns from the blocky grains revealed metal peaks (suboxide peaks are close to those of the metal phase) and tetragonal oxide peaks (but no monoclinic peaks). Dark-field micrographs were taken using these tetragonal peaks and reveal the fine particles seen in Fig. 9. Fig. 9 shows one bright-field and two dark-field images from the suboxide region of Zr–2.5Nb alloy oxide formed in pure water. The bright field image in Fig. 9(a) shows

the oxide/metal interface (dotted line) with the oxide and sub-oxide on either side. Fig. 9(b) shows a dark-field image taken using the $(101)_T$ reflection indicated in the diffraction pattern shown in Fig. 9(c). Fig. 9(d) is a dark-field image taken using the $(200)_T$ reflection shown in the diffraction pattern Fig. 9(e). Small crystallites appear in the rectangular grains in the sub-oxide region in both of these dark field images, with different crystallites lighting up depending on the dark-field reflection used.

The presence of these crystallites is coincident with the region where the oxygen content is greater than ~30%. One possibility is that as the oxide advances some oxygen diffuses into the metal just ahead of the advancing front and forms the suboxide phase. Because the solubility limit of the suboxide phase is ~29 at.%, the remainder of the oxygen precipitates as ZrO_2. Since these precipitates are small, and possibly sub-stoichiometric, the tetragonal phase is favored over the monoclinic phase [15,16]. Due to the relatively few observations, it is possible that this could be an experimental artifact, caused, for example, by small grains of oxide being transferred into the metal during mechanical polishing.

Fig. 10 shows bright-field, and dark-field images of the suboxide region of Zircaloy-4 oxide formed in pure water. The bright-field image (Fig. 10(a)) shows large metal grains in the bottom-left side of the image and some columnar oxide grains in the

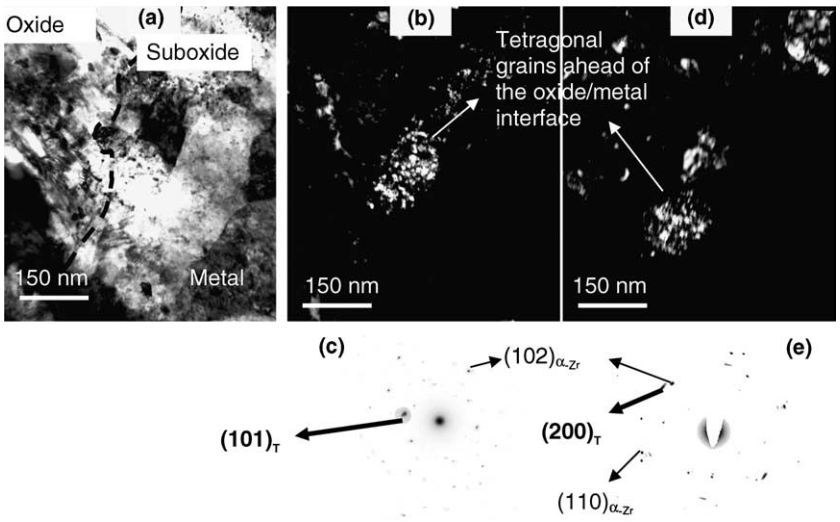

Fig. 9. Oxide tetragonal grains within the blocky 'suboxide' grains at the oxide/metal interface of Zr–2.5Nb oxide formed in 360 °C pure water environment. (a) Bright-field image, (b) dark-field image, (c) electron diffraction pattern using $(101)_T$ reflection, (d) dark-field image, (e) electron diffraction pattern using $(200)_T$ reflection.

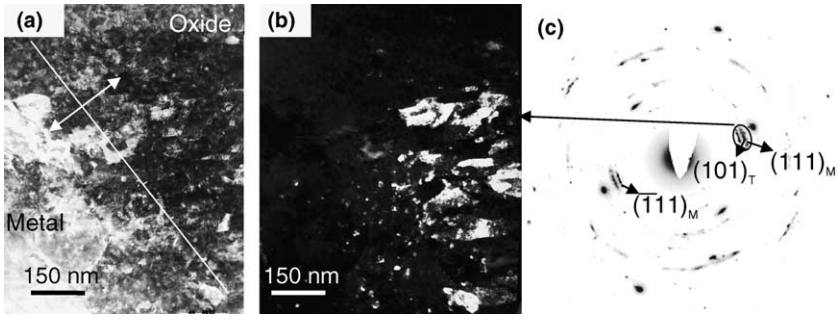

Fig. 10. Both columnar and equiaxed grains at the oxide/metal interface of Zircaloy-4 oxide formed in pure water. (a) Bright-field image from the oxide/metal interface region. Line with arrows shows the approximate location of the oxide/metal interface. (b) Dark-field image from the same region using $(\bar{1}11)_M$–$(101)_T$–$(111)_M$ reflections, (c) electron diffraction pattern from the oxide/metal interface.

top-right side of the image. There is no distinct oxide/metal interface in the image. The dark-field image shown was taken with the aperture enclosing the $(\bar{1}\,1\,1)_M$, $(1\,0\,1)_T$ and $(1\,1\,1)_M$ reflections in the diffraction pattern. In the dark-field image both equiaxed and columnar type of oxide grains appear. However, the columnar grains appear primarily on the right side of the image and equiaxed grains appear only in the left side (vicinity of the metal grains) of the image.

No segregation of alloying elements is observed at the oxide/metal interface for any of the alloying elements (Sn, Cr, Nb, Fe) in any of the alloy oxides studied, in agreement with previous observations in similar oxides using synchrotron radiation microbeam X-ray fluorescence [2,3]. This only refers to segregation on the scale of a few tenths of microns (e.g. to the oxide/metal interface), and does not rule out the possibility of nanoscale segregation to oxide grain boundaries as observed in [17,18].

3.5. Incorporation of second-phase precipitates

The incorporation of second-phase precipitates was also examined in the oxide layers formed on Zircaloy-4, ZIRLO and Zr–2.5Nb alloys in pure water. Second-phase precipitates were incorporated in unoxidized form into the oxide layer. Many metallic second-phase precipitates were observed in the oxide near the oxide/metal interface. After a certain distance from the oxide/metal interface into the oxide layer, both amorphous and oxidized second-phase precipitates were found. The differences in the second-phase precipitate oxidation for the different alloys are discussed in this section in more detail.

Fig. 11(a)–(c) shows three different second-phase precipitates incorporated in the oxide layer of ZIRLO formed in pure water. In this alloy, only β-Nb precipitates were detected in the oxide layer. All precipitates observed within 550 nm of the oxide/metal interface were crystalline, and beyond that distance all observed precipitates were amorphous. The Zr–Nb–Fe second-phase precipitates in ZIRLO were not observed in the oxide. These Zr–Nb–Fe precipitates are larger than the β-Nb precipitates and more widely spaced, thereby making detection more difficult. Additional work is required to determine how they are incorporated in the oxide layer.

Fig. 12(a)–(c) shows three different second-phase precipitates observed in a growing Zr–2.5Nb alloy oxide formed in water: one precipitate is in the metal region, and two are incorporated in the oxide, crystalline at first, and amorphous, further into the layer. The crystalline precipitates are β-Nb. Second-phase precipitates are incorporated in the oxide in metallic form (Fig. 12(b)) and at about 800 nm away from the oxide/metal interface, all observed precipitates are amorphous (Fig. 12(c)). Upon tilting, these amorphous precipitates do not change their contrast. The crystalline second-phase precipitates incorporated into the oxide exhibited cracks on the side away from the oxide/metal interface, as seen in Figs. 11(a) and 12(b). It is possible that the cracks are formed during sample preparation as a result of accumulated stresses which cause foil buckling. Since the amorphous precipitates do not show these cracks, it is possible that the amorphization of the precipitates and associated loss of alloying elements causes some of these residual stresses to disappear.

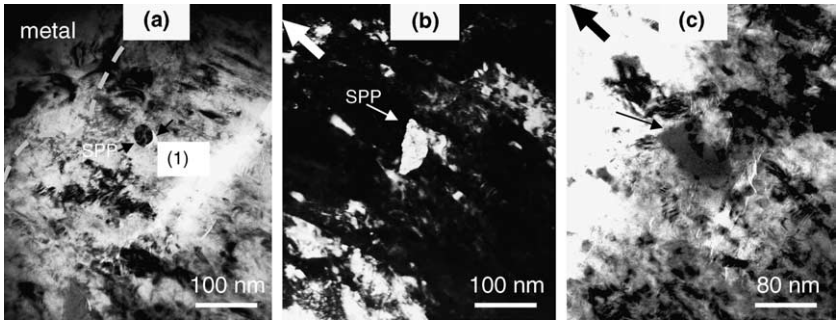

Fig. 11. Incorporation of second-phase precipitates in ZIRLO oxide. (Arrows show the oxide growth direction.) (a) Crystalline second-phase precipitate in the oxide layer (60 nm away from oxide/metal interface), (1) crack observed near precipitate on side away from the oxide/metal interface, (b) crystalline second-phase precipitate in the oxide (500 nm away from oxide/metal interface), (c) amorphous ZrNb second-phase precipitate in the oxide layer. The large black arrows on the upper left of (b) and (c) show the oxide growth direction.

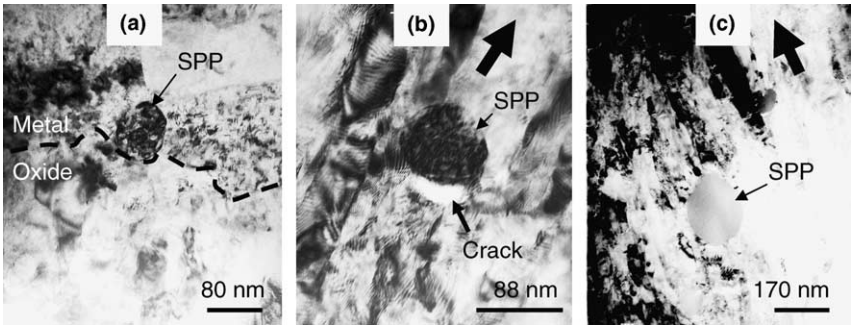

Fig. 12. Second-phase precipitate in Zr–2.5Nb. (a) Second-phase precipitate in the metal, (b) crystalline second-phase precipitate in the oxide layer, (c) amorphous second-phase precipitate in the oxide layer. (Arrows show the oxide growth direction.)

The amorphous precipitates appear to dissolve far from the oxide/metal interface. Fig. 13 shows a bright-field transmission electron micrograph from the outer part of the Zr–2.5Nb alloy oxide formed in pure water. In the micrograph, two partially dissolved second-phase precipitates are shown. The appearance of these precipitates is different from the amorphous precipitates shown in Fig. 12(c). While the precipitate/oxide boundary is sharp in Fig. 12(c), the interface is diffuse and discontinuous in Fig. 13. The EDS spectra from these precipitates show both Nb and Zr, and there is no compositional difference between amorphous and dissolved amorphous precipitates.

The second-phase precipitates observed in Zircaloy-4 are consistent with previous observations, i.e. $Zr(Cr,Fe)_2$ Laves phase precipitates with C14 hcp structure [19]. Fig. 14 shows bright-field and dark-field images from a second-phase precipitate found 1 μm from the oxide/metal interface in the oxide layer of Zircaloy-4. Partially oxidized second-phase precipitates are observed in the oxide. As indicated in Fig. 14(a), two small regions of the second-phase precipitate appear to be crystalline and metallic looking. These regions appear in the dark-field image shown in Fig. 14(b) from one of the metal reflections. The region in between the metallic-looking parts of the second-phase precipitate is identified as oxide. This region exhibits small crystallites and the electron diffraction pattern shows a reflection associated with tetragonal ZrO_2, again indicating the stabilization of tetragonal zirconia by small crystallites. Energy dispersive point spectra taken from the metallic looking region and from the oxidized precipitate region show that both regions contain Zr, Fe and Cr. However, the metallic-looking region has a higher Fe/Cr ratio than the oxidized region.

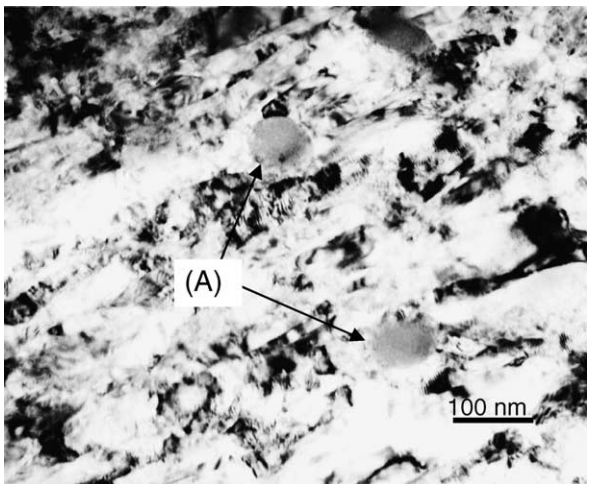

Fig. 13. Partially dissolved amorphous second-phase precipitates in Zr–2.5Nb alloy oxide formed in pure water (A).

4. Discussion

The present observations are discussed and compared to previous TEM observations and to other information previously obtained from these same alloy oxides (corrosion kinetics and other characterization, such as microbeam X-ray diffraction and X-ray fluorescence techniques at APS synchrotron facility at ANL and transmitted light optical microscopy). The observations can be divided into (i) morphology and texture of the oxide, (ii) oxide/metal interface region and (iii) incorporation of second-phase precipitates.

The grain morphology in the oxide layers consists of columnar and equiaxed grains. The columnar grains had different widths/lengths depending on the alloy. The oxide microstructure seen in the bulk of the alloy oxide was observed to extend to

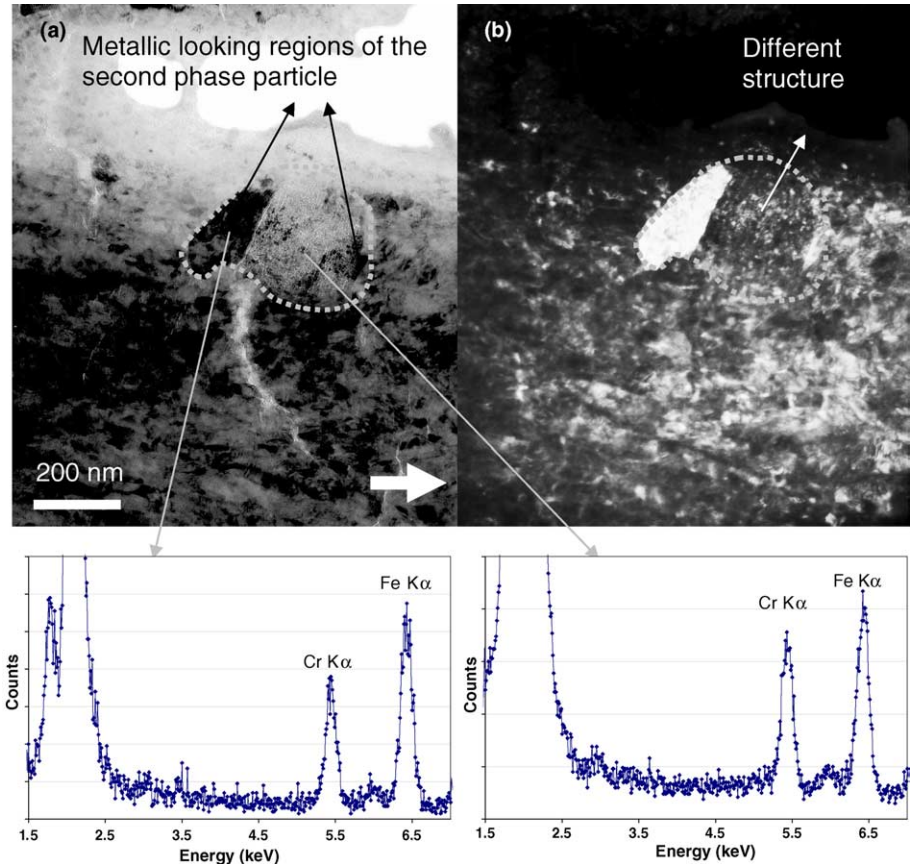

Fig. 14. (a) Bright-field and (b) dark-field images from the second-phase precipitate found 1 μm away from the oxide/metal interface in the oxide layer of Zircaloy-4 (arrow shows the oxide growth direction). Energy dispersive spectra collected from the metallic-looking region and the oxidized region are also shown.

the oxide/metal interface, e.g. columnar grains in the Zr–2.5Nb alloy, whereas the oxide/metal interface in ZIRLO and Zircaloy-4 had a higher percentage of equiaxed grains. The oxide/water interface in contrast, had a higher percentage of equiaxed grains in all alloys.

Periodic lateral cracking was observed, with a period similar to that observed using other techniques. Small equiaxed grains were associated with these cracks. The interpretation of these observations is that the oxide first forms in small equiaxed grains, out of which a few grains (properly oriented to minimize stress) grow and become columnar grains. These columnar grains have the $(200)_M$ pole aligned close to the direction of growth, which minimizes the stress in the oxide, [20,21]. At transition, the oxide loses protectiveness, the nucleation rate increases, and a new layer is formed composed of small equiaxed grains. These grains again grow into columnar grains, creating the observed alternation of columnar and equiaxed layers. During sample preparation, cracks form preferentially in the regions with small grains, either because of the higher density of grain boundaries or because the ion milling rate is faster in these regions. Thus, it is thought that the higher concentration of equiaxed grains causes the cracks rather than the reverse. Fig. 3(d) supports this interpretation, since it shows a variation of columnar to equiaxed to columnar grains, without any apparent cracks.

A periodic structure in oxide growth has not been commonly reported in the TEM literature, although the periodic nature of the corrosion process has been recognized by various researchers [6,9,11,22]. One of the possible reasons is that the amount of thin area in TEM samples is commonly smaller than the length of the periods, so that these become difficult to detect. However, many researchers have reported other observations which are consistent with the current observations. For example, equi-

axed grains are often observed near the cracks in the oxide layers [6,9,22]. The type of structure seen in Fig. 3(d), with many equiaxed grains observed between two columnar grain containing regions was also observed in transmission electron microscopy by Doriot [11] in Zr–1NbO alloy oxide formed in steam. Many researchers (e.g. [4,6,7,9,22]) have reported columnar oxide grains in the pre-transition oxides. Therefore, the current observations are in reasonable agreement with previous studies.

The periodic structure in the oxide layers of the current materials was also made evident by other techniques, as shown in Table 2. For example, the $(1\,0\,1)_T$ peak intensity in micro X-ray diffraction patterns was observed to vary periodically in the oxide layer and its periodicity was out of phase with $(0\,2\,0)_M$ [3]. The current TEM observations indicate that the fraction of tetragonal phase is higher where small equiaxed grains are observed in the oxide layer, which is also where the crack density is high and where monoclinic grains are not aligned.

It has been previously observed that alloys with good corrosion resistance exhibit wide and long columnar oxide grains while less corrosion resistant alloys exhibit more equiaxed and short and narrow columnar oxide grains [4–6,8,22]. The current study further shows that these large columnar grains in Zr–2.5Nb have a smaller degree of grain-to-grain misalignment than the smaller columnar grains formed in the other alloys.

It is not immediately apparent how the alloy differences can cause the observed variation in oxide grain size. It is possible that the initial equiaxed grain population from which the columnar grains are created is different between the alloys, because of different nucleation rates of the new oxide. Another possibility is that solute segregation to the oxide/oxide grain boundaries occurs during oxide growth [17,18], in which case the higher the solute content in the matrix, the smaller the grains formed. The observations in this study are roughly in agreement with this last hypothesis because the smallest grains are observed in Zircaloy-4 (1.5%Sn in solid solution), followed by ZIRLO (which contains a total of 1%Sn + 0.4%Nb in solution), and by Zr–2.5Nb (0.4%Nb in solution). The amounts in solid solution are calculated from the binary phase diagram, so they are likely not exact, but the overall trend is for increasing oxide grain size with decreasing solute concentration in the matrix. However, this is not the sole factor, as pure Zr with low solute content exhibits poor corrosion behavior [23].

Although a systematic study of the influence of environment on oxide structure was not conducted in this study, oxides formed in Zr–2.5Nb in water and in lithiated water (Fig. 5) were studied. While Zr–2.5Nb alloy oxide formed in pure water shows columnar grains that are long, wide, and well-oriented with respect to each other, the micrograph of the oxide layer formed in lithiated water shows mainly equiaxed and short-narrow columnar grains. This observation is also in agreement with the observations of Pecheur et al. [7]. It is commonly observed that the corrosion rate of Zr alloys is accelerated in lithiated water [7,24,25]. Pecheur et al. [7] examined Zircaloy-4 alloy oxide formed in 70 ppm Li water using transmission electron microscopy. They observed that before the strong enhancement of the oxidation rate, the oxide grains are columnar grains and the Li concentration is higher in the outer oxide but lower near the oxide/metal interface. However, after the strong enhancement of the oxidation rate, the grain structure exhibits only equiaxed grains near the oxide/metal interface and the Li concentration is higher throughout the oxide. The authors believe that the ingress of Li weakens the intergranular cohesion and allows easy transport of oxygen.

On the oxide side of the oxide/metal interface region, the many observations can be summarized in that the columnar grains advance right to the interface and that a well-developed texture starts at the interface and is marked in the bulk. The metal region just ahead of the oxide exhibits higher oxygen content than the bulk of the metal and contains small precipitates of tetragonal oxide. The overall composition measurement in that region shows a concentration of oxygen above the solubility limit, which is interpreted as the combination of a matrix saturated (29 at.%) with dissolved oxygen (the sub-oxide phase Zr_3O) and precipitates of tetragonal Zr which increase the overall oxygen content. A hexagonal Zr_3O phase was observed by Iltis and Michel [26] in a narrow spatial domain located near the oxide/metal interface of Zircaloy-4 oxide. Anada and Takeda [9] studied the metal side of the oxide/metal interface in TEM. In pre-transition oxides of Zircaloy-4, Zircaloy-2 and Zircaloy-4 with 1%Nb, they observed two layers: 50–80 nm thick layers of tetragonal ZrO_2 grains near the oxide/metal interface and a 200 nm thick sub-stoichiometric oxide layer containing 'distorted' monoclinic ZrO_2 and α-Zr, containing also 10 nm equiaxed oxide grains, consistent with the present observations.

Using TEM Bossis et al. [27] and Foord and Newcomb [18] observed a hexagonal ω-Zr structure at the oxide/metal interface of Zircaloy-4 formed in steam. This structure contained a significant amount of oxygen. Even though these observations in the literature do not agree exactly with what was observed in this study, they show that a different complex structure forms at the oxide/metal interface other than the structure of bulk oxide and bulk metal. As mentioned previously, the different 'sub-oxide' layer thicknesses observed in this work could be related to an alloy effect or to different stages in the corrosion process at which the samples were archived. It is impossible from the data we have to resolve the issue, and further work would be useful to understand these differences.

The second-phase precipitates are incorporated in metallic form in the oxide, in agreement with previous studies. Later in the oxide layer, these precipitates appear either in the form of small oxide crystallites or amorphous. Both types of precipitates in the oxide layer had been observed previously [19,28]. The oxide crystallites formed on the precipitates in Zircaloy-4 have a higher content of tetragonal oxide than the bulk oxide, and this observation is confirmed here. In the case of amorphous precipitates, it is thought that the previously crystalline β-Nb precipitates become amorphous because the sudden ingress of oxygen into the precipitates causes metal–oxygen bonds to form that, while respecting short range order, form too quickly to obey long range order.

The ensemble of these observations is self-consistent, in good agreement with previous observations and allows for the development of a model for oxide growth which needs to be verified by detailed studies.

5. Conclusion

A detailed transmission electron microscopy study using cross-sectional samples was conducted to discern the differences between the structures of oxides formed in different alloys and rationalize differences in corrosion kinetics. The main conclusions are as follows:

- A periodic cracking pattern is observed in the oxide that shows, about the same period as previously observed in using microbeam synchrotron radiation and as determined from the corrosion rate changes. Evidence of a layered columnar–equiaxed–columnar structure was seen.
- Both equiaxed and columnar grains are observed in the oxide layers. The equiaxed grains are in regions where there is a higher content of tetragonal zirconia and the columnar grains are monoclinic. Large columnar grain size is observed in oxides with low corrosion rates. The grain morphology differs from alloy to alloy and the grain size increases as the corrosion rate decreases. Both monoclinic and tetragonal oxides are observed and the tetragonal oxide is normally associated with small (equiaxed) grains.
- The monoclinic oxide texture changes within the oxide layer right from the oxide/metal interface to a well-developed structure further from the interface with the poles of the $(200)_M$ planes aligned nearly parallel to the oxide growth direction. The overall texture agrees with previous observations. As the grain-to-grain alignment between columnar grains becomes more perfect, the corrosion rate decreases.
- An interface region is observed in the metal just ahead of the oxide which has higher oxygen content than the bulk of the metal. This region shows a different contrast in bright-field than the grains in the bulk of the metal and shows small tetragonal oxide grains, in the region where the solubility of oxygen in hcp-Zr is exceeded.
- Second-phase precipitates are incorporated into the oxide in metallic form and later become oxidized. The β-Nb precipitates in ZIRLO and Zr–2.5Nb become amorphous within the layer and eventually dissolve. The $Zr(Cr,Fe)_2$ precipitates in Zircaloy-4 form oxide crystallites with a higher percentage of tetragonal phase.

Acknowledgements

The authors would like to thank George Sabol and Randy Lott for many lively discussions. This work was supported by a DOE-NERI grant number DE-FC03-99SF21918 and by a DOE I-NERI grant number DE-FG07-03RL14530.

References

[1] IAEA, Waterside Corrosion of Zirconium Alloys in Nuclear Power Plants. IAEA-TECDOC-996, Vienna, 1998.
[2] A. Yilmazbayhan, A.T. Motta, R.J. Comstock, G.P. Sabol, B. Lai, Z. Cai, J. Nucl. Mater. 324 (1) (2004) 6.
[3] A.T. Motta, A. Yilmazbayhan, R.J. Comstock, J.M. Partezana, G.P. Sabol, B. Lai, Z. Cai, J. ASTM Int. 2 (5) (2005), Paper ID JAI-12375.

[4] F. Garzarolli, H. Seidel, R. Tricot, J. P. Gros, in: Zirconium in the Nuclear Industry: 9th International Symposium, ASTM STP, vol. 1132, 1991, p. 395.
[5] G.P. Sabol, S.G. McDonald, G.P. Airey, in: Zirconium in Nuclear Applications, ASTM STP, vol. 551, 1974, p. 435.
[6] B. Wadman, Z. Lai, H.-O. Andren, A.-L. Nysrom, P. Rudling, H. Pettersson, in: Zirconium in the Nuclear Industry: 10th International Symposium, ASTM STP, vol. 1245, 1994, p. 579.
[7] D. Pecheur, J. Godlewski, P. Billot, J. Thomazet, in: Zirconium in the Nuclear Industry: 11th International Symposium, ASTM STP, vol. 1295, 1995, p. 94.
[8] H. Anada, B.J. Herb, K. Nomoto, S. Hagi, R.A. Graham, T. Kuroda, in: Zirconium in the Nuclear Industry: 11th International Symposium, ASTM STP, vol. 1295, 1996, p. 74.
[9] H. Anada, K. Takeda, in: Zirconium in the Nuclear Industry: 11th International Symposium, ASTM STP, vol. 1295, 1996, p. 35.
[10] G.P. Sabol, G.R. Kilp, M.G. Balfour, E. Roberts, in: Zirconium in the Nuclear Industry: 8th International Symposium, ASTM STP, vol. 1023, 1989, p. 227.
[11] S. Doriot, Unpublished Research, CEA/SRMA, 2003.
[12] J.L. Béchade, R. Dralet, P. Goudeau, P. Yvon, Mater. Sci. Forum 347–349 (2000) 471.
[13] J.L. Béchade, P. Goudeau, M. Bessiere, P. Yvon, International Conference on Residual Stresses-5 (1997) 331.
[14] J.L. Béchade, P. Goudeau, M. Gailhanou, P. Yvon, High Temp. Mater. Processes 2 (1998) 359.
[15] R.C. Garvie, J. Phys. Chem. 69 (4) (1965) 1238.
[16] H. Tomaszewski, K. Godwod, J. Eur. Ceramic Soc. 15 (1995) 17.
[17] K. Takeda, H. Anada, in: Zirconium in the Nuclear Industry: 12th International Symposium, ASTM STP, vol. 1354, 2000, p. 592.
[18] D.T. Foord, S.B. Newcomb, in: Proceedings of the Third International Conference on the Microscopy of Oxidation, Cambridge, UK, 1997, p. 488.
[19] D. Pecheur, F. Lefebvre, A.T. Motta, C. Lemaignan, J.-F. Wadier, J. Nucl. Mater. 189 (1992) 318.
[20] N. Petigny, P. Barberis, C. Lemaignan, Ch. Valot, M. Lallemant, J. Nucl. Mater. 280 (2000) 318.
[21] H. Li, M.G. Glavicic, J.A. Szpunar, Mater. Sci. Eng. A336 (2004) 164.
[22] H.-J. Beie, A. Mitwalsky, F. Garzarolli, H. Ruhmann, H.-J. Sell, in: Zirconium in the Nuclear Industry: 10th International Symposium, ASTM STP, vol. 1245, 1994, p. 615.
[23] S. Kass, ASTM STP, vol. 368, 1964, p. 3.
[24] N. Ramasubramanian, N. Precoanin, V.C. Ling, in: Zirconium in the Nuclear Industry: 8th International Symposium, ASTM STP, vol. 1023, 1989, p. 187.
[25] R.A. Perkins, R.A. Busch, in: Zirconium in the Nuclear Industry: 9th International Symposium, ASTM STP, vol. 1132, 1991, p. 595.
[26] X. Iltis, H. Michel, J. Alloys Comp. 177 (1991) 71.
[27] P. Bossis, G. Lelievre, P. Barberis, X. Iltis, F. Lefebvre, in: Zirconium in the Nuclear Industry: 12th International Symposium, ASTM STP, vol. 1354, 2000, p. 918.
[28] D. Pecheur, F. Lefebvre, A.T. Motta, C. Lemaignan, D. Charquet, in: Zirconium in the Nuclear Industry: 10th International Symposium, ASTM STP, vol. 1245, 1994, p. 687.